JOURNAL OF GUIDANCE, CONTROL, AND DYNAMICS
Vol. 16, No. 6, November–December 1993

# Classical and Robust $H_\infty$ Control Redesign for the Hubble Space Telescope

Bong Wie* and Qiang Liu†
*Arizona State University, Tempe, Arizona 85287*
and
Frank Bauer‡
*NASA Goddard Space Flight Center, Greenbelt, Maryland 20771*

**A control redesign problem of the Hubble Space Telescope for reducing the effects of solar array vibrations on telescope pointing jitter is investigated. Both classical and $H_\infty$ control design methodologies are employed for such a control problem with a noncollocated actuator and sensor pair. This paper successfully demonstrates the effectiveness of a dipole concept for precision line-of-sight pointing control in the presence of significant structural vibrations. Proposed controllers with two dipoles effectively reduce the effects of the solar array induced disturbances at 0.12 and 0.66 Hz on pointing jitter.**

## I. Introduction

THE Hubble Space Telescope (HST), illustrated in Fig. 1, is a 13-ton free-flying spacecraft with a precision pointing stability requirement of 0.007 arc-s over a 24-h period, which is the most stringent pointing requirement imposed on any spacecraft to date.[1,2]

Following the successful deployment of the HST from the Space Shuttle Orbiter in April 1990, the HST has been experiencing a pointing jitter problem caused by the unexpected solar array induced disturbances. According to Ref. 3, there appear to be two types of thermal flutter of the 20-ft-long solar arrays: 1) an end-to-end bending oscillation at 0.12 Hz when the spacecraft passes between sunlight and shadow and 2) a sideways bending oscillation at 0.66 Hz that occurs on the day side of the Earth. Under the worst conditions, the tips of the two 20-ft arrays could deflect as much as 3 ft. The effect of such solar array oscillations is that the telescope moves 0.00022 in., enough to make the planned long observations of as much as 25 min not worthwhile.

Although reprogramming the onboard digital control logic has been successful in reducing the effects of the 0.12-Hz solar array oscillations on jitter, the 0.66-Hz jitter problem is still to be resolved.[4] In this paper, a control redesign problem for reducing the effects of both 0.12- and 0.66-Hz solar array oscillations on jitter is investigated. It is shown that proposed controllers with two disturbance rejection dipoles effectively accommodate the persistent disturbances at both 0.12 and 0.66 Hz.

The remainder of this paper is organized as follows. In Sec. II, the HST pointing control system is briefly reviewed, and a control redesign problem is formulated. In Sec. III, a classical frequency-domain design technique is employed to redesign the HST pointing control system. In Sec. IV, a robust $H_\infty$ control design technique is employed to demonstrate the usefulness and practicality of such a modern approach to control design. The concept of internal modeling of a persistent disturbance is exploited for both techniques, introducing a model of the disturbance into the feedback loop. Classical and robust $H_\infty$ control design techniques used in this paper are briefly summarized in Appendices A and B, respectively.

## II. Problem Statement for Hubble Space Telescope Control Redesign

The pointing control system of the HST consists of fine-guidance sensors, star trackers, rate gyros, reaction wheels, magnetic torquers, and a digital computer. The rate gyro assembly comprises six rate integrating gyros and provides rate and attitude information that is supplemented by attitude data from star trackers and fine-guidance sensors.[1,2] Magnetic torquers are used for momentum management. Control torques are provided by the four skewed reaction wheels that are not collocated with the rate gyro assembly. The rate gyros are located with the star tracker on an equipment shelf on the back side of the optical telescope assembly, whereas the reaction wheels are located at the midsection of the main body, as can be seen in Fig. 1. As a result, the primary bending modes of the optical telescope assembly have large negative modal gains (see Table 1) and they are interacting "unstably" with

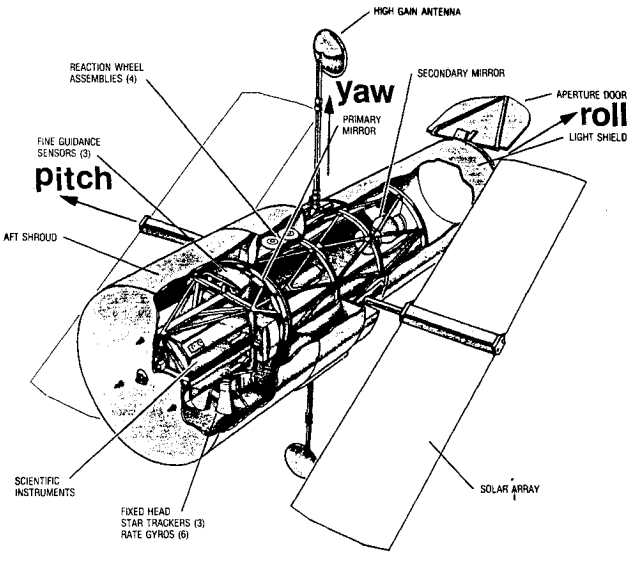


**Fig. 1 Hubble Space Telescope.**

Received Feb. 11, 1992; revision received Oct. 15, 1992; accepted for publication Jan. 22, 1993. 

*Professor, Department of Mechanical and Aerospace Engineering. Associate Fellow AIAA.

†Graduate Research Assistant, Department of Mechanical and Aerospace Engineering; currently at the American GNC Corporation, CA. Student Member AIAA.

‡Associate Head, Guidance and Control Branch. Member AIAA.

the pointing control system. (The pointing control problem of the HST is thus an excellent practical example of the so-called noncollocated control problem of flexible structures.[5-10])

Detailed descriptions of the HST pointing control system, performance analyses, and ground-test results can be found in Refs. 1 and 2. Recent flight results associated with the pointing jitter problem caused by the solar array oscillations can be found in Refs. 3 and 4. In this paper, we consider only the pitch-axis control design problem, which has most significant interaction with the solar arrays. (The roll, pitch, and yaw control axes of the HST, illustrated in Fig. 1, are aligned with the principal axes of the vehicle.)

The pitch-axis transfer function of the HST is given by

$$\frac{\theta(s)}{u(s)} = \frac{1}{Is^2} + \sum_{i=1} \frac{K_i/I}{s^2 + 2\zeta\omega_i s + \omega_i^2} \tag{1}$$

where $\theta$ is the pitch-axis pointing error output, $u$ the pitch-axis reaction wheel control torque input, $s$ the Laplace transform variable, $I = 77{,}076$ kg-m$^2$ the spacecraft pitch inertia, $K_i$ the $i$th flexible mode gain in the pitch axis, $\omega_i$ the $i$th flexible mode frequency in rad/s, and $\zeta$ the passive damping ratio assumed as 0.005.

Table 1 lists the pitch-axis modal data of the HST, and the corresponding transfer function zeros in rad/s are

$$-0.0034 \pm 0.6850j, \quad -0.0134 \pm 2.6983j$$

$$-0.0272 \pm 5.5805j, \quad -0.3397 \pm 67.945j$$

$$-0.3790 \pm 75.818j, \quad -0.4255 \pm 85.079j$$

$$-0.4464 \pm 89.286j, \quad -0.4780 \pm 95.589j$$

$$-58.678, \quad +59.069$$

The transfer function with "nonalternating" poles and zeros has a nonminimum-phase zero at $s = 59.069$ since the rate gyros are not collocated with the reaction wheels, as can be seen in Fig. 1.

Figure 2 shows a simplified pitch-axis block diagram of the HST pointing control system. The outer loop with the fine-guidance sensor and a command generator for the feedforward path are not shown here. Other axes of the HST employ the same control architecture.

The original controller on board the HST, which is basically a digital proportional-integral-derivative (PID) controller with $K_P = 9$, $K_I = 0.05$, and $K_D = 0.5$, utilizes a finite impulse response (FIR) filter in the rate path to attenuate the high-frequency, main-body (optical telescope assembly) bending modes.

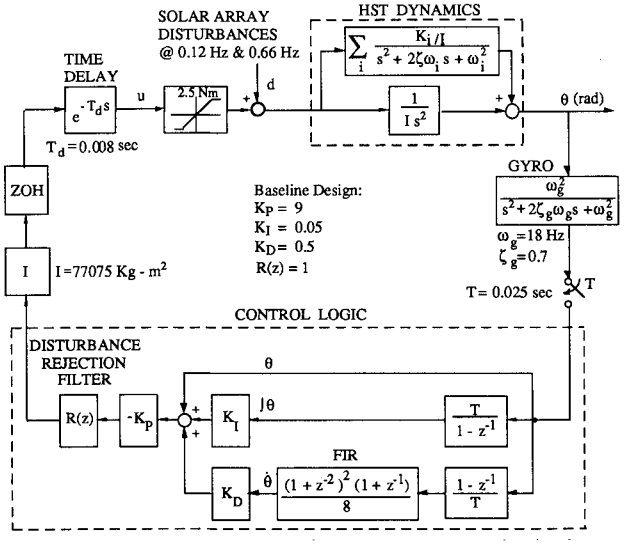


**Fig. 2 Simplified block diagram of the HST pitch-axis pointing control system.**

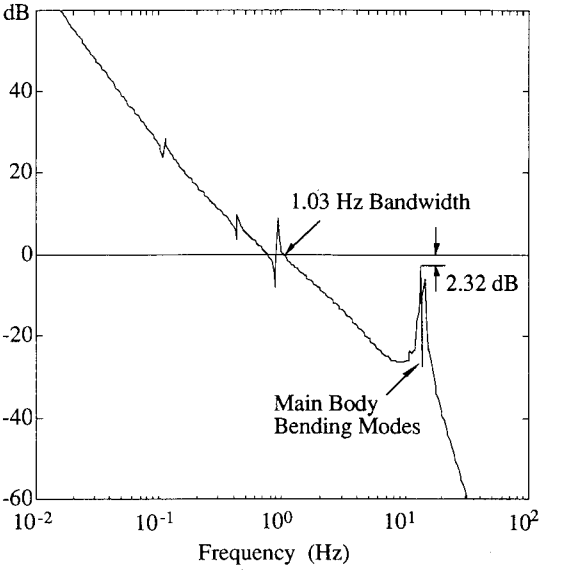


**Fig. 3 Bode magnitude plot of the loop transfer function of the original HST control design.**

**Table 1 HST modal data for the pitch axis**

| Mode number | $\omega_i$, Hz | Modal gain, $K_i$ | Description |
|---|---|---|---|
| 1 | 0.110 | 0.018 | Solar array |
| 2 | 0.432 | 0.012 | High-gain antenna |
| 3 | 0.912 | 0.057 | Aperture door |
| 4 | 10.834 | 0.024 | Telescope structure |
| 5 | 12.133 | 0.155 | Telescope structure |
| 6 | 13.201 | −1.341 | Telescope structure |
| 7 | 14.068 | −1.387 | Telescope structure |
| 8 | 14.285 | −0.806 | Telescope structure |
| 9 | 15.264 | −0.134 | Telescope structure |

The solar array induced disturbances are modeled as

$$d(t) = A_1\sin(p_1 t + \phi_1) + A_2\sin(p_2 t + \phi_2) \tag{2}$$

where the frequencies in rad/s are known as

$$p_1 = 2\pi(0.12)$$
$$p_2 = 2\pi(0.66) \tag{3}$$

The magnitudes $A_i$ and phases $\phi_i$ are unknown for control design, whereas the nominal magnitudes have been estimated as $A_1 = A_2 = 0.2$ N-m, from flight results.[4]

The Bode magnitude plot of the loop transfer function of the original controller on board the HST is shown in Fig. 3. As can be seen in this figure, the pitch-axis pointing control system with the original controller has a 1.03-Hz gain crossover frequency. The FIR filter in the rate path provides 2.3-dB gain suppression of the 13.2-Hz bending mode. The solar array induced disturbances for this controller lead to pointing jitter of 0.1-arc-s peak, which significantly exceeds the 0.007-arc-s pointing accuracy requirement.

Thus, a new digital control logic is to be designed to most effectively attenuate the effects of the solar array oscillations at 0.12 and 0.66 Hz. An integral compensation is also needed to attenuate gravity gradient and aerodynamic disturbances. The control redesign requirements and/or goals can be stated as follows[4]:

1) Maintain at least 5-dB gain margin and 20-deg phase margin.

2) Provide at least 6-dB gain suppression (roll off) of the high-frequency telescope structural modes at 14 Hz.

3) Provide at least 20-dB additional disturbance attenuation at both 0.12 and 0.66 Hz with respect to the original design.

4) Maintain the bandwidth (the open-loop gain crossover frequency) close to 1.5 Hz.

In the next section we will present a classical control redesign for the HST, followed by a modern $H_\infty$ control redesign, to reduce the effects of solar array vibrations on telescope pointing jitter. Both designs will be compared to the original controller on board the HST, and some practical usefulness of a modern design technique that deals with both structured and unstructured uncertainties will also be demonstrated. In this paper, theoretical aspects of robust control design will not be elaborated, although some detailed discussion on both the classical and robust $H_\infty$ design techniques can be found in the Appendices.

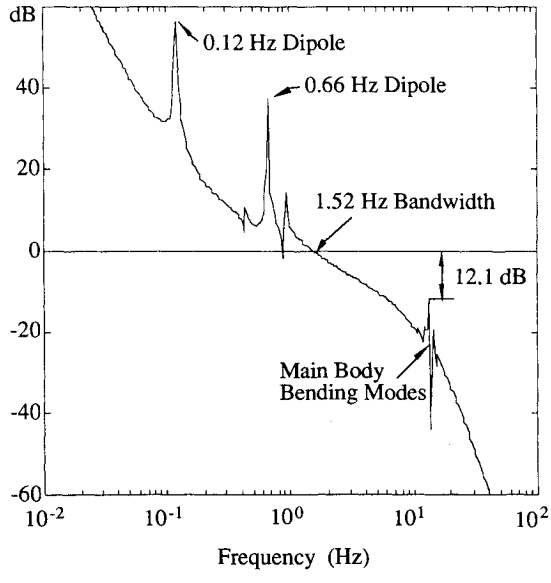


**Fig. 4 Bode magnitude plot of the loop transfer function of a classical control redesign.**

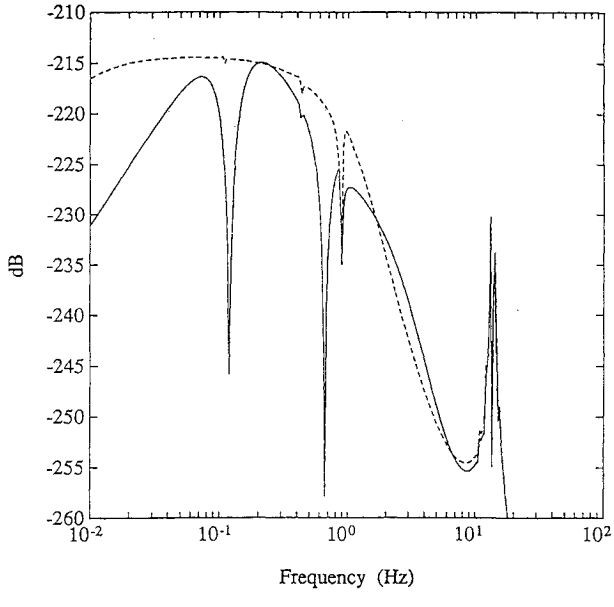


**Fig. 5 Closed-loop frequency magnitude response of a classical control redesign.**

## III. Classical Control Design

For the classical $s$-domain synthesis of digital control logic, the computational delay and the sample/zero-order-hold (ZOH) delay, shown in Fig. 2, are first approximated as

$$e^{-0.008s} \approx \frac{(0.008s)^2/12 - 0.008s/2 + 1}{(0.008s)^2/12 + 0.008s/2 + 1} \tag{4}$$

$$\frac{1 - e^{-0.025s}}{0.025s} \approx \frac{1}{(0.025s)^2/12 + 0.025s/2 + 1} \tag{5}$$

Following a classical design procedure described in Appendix A, a new controller was designed to accommodate the disturbances at 0.12 and 0.66 Hz. After a trial-and-error iteration, a PID controller for the control logic architecture shown in Fig. 2 was found as $K_P = 7.720$, $K_I = 0.492$, and $K_D = 0.948$. This controller utilizes the same FIR filter as in the original controller and employs a periodic-disturbance rejection filter of the form

$$R(s) = \frac{[(s/z_1)^2 + 2\zeta_{z_1}s/z_1 + 1]}{[(s/p_1)^2 + 1]} \frac{[(s/z_2)^2 + 2\zeta_{z_2}s/z_2 + 1]}{[(s/p_2)^2 + 1]} \tag{6}$$

where

$$z_1 = 2\pi(0.124), \quad \zeta_{z_1} = 0.364$$

$$p_1 = 2\pi(0.120)$$

$$z_2 = 2\pi(0.612), \quad \zeta_{z_2} = 0.127$$

$$p_2 = 2\pi(0.660)$$

To alleviate numerical problems associated with the direct realization for digital implementation, as discussed in Refs. 3 and 4, this fourth-order filter should be first transformed into two second-order filters in parallel and then discretized.

This new PID controller with two dipoles satisfies the 1.5-Hz gain crossover frequency requirement, as well as the gain and phase margin requirements. However, the FIR filter in the rate path does not provide enough gain attenuation for the high-frequency bending modes. The high-frequency structural modes near 14 Hz are, in fact, phase stabilized by the phase lag effects of the control system. Consequently, the second requirement of gain stabilizing the primary structural bending modes at 14 Hz has not been met, although all of the other design requirements and goals have been satisfied.

Notch filtering of the significantly interacting modes at 14 Hz was tried following the classical control design procedure described in Appendix A, resulting in the following controller:

$$K(s) = 7.72(1 + 0.492/s + 0.948s)R(s)S(s) \tag{7}$$

where $R(s)$ is the same periodic-disturbance rejection filter as given in Eq. (6) and

$$S(s) = \frac{[(s/87)^2 + 2(0.001)s/87 + 1]}{[(s/45)^2 + 2(0.70)s/45 + 1]} \tag{8}$$

where $S(s)$ is referred to as the structural filter.

As can be seen in the Bode magnitude plot of the loop transfer function (Fig. 4), the controller given by Eq. (7) has a 1.5-Hz gain crossover frequency. The closed-loop system with this controller has a phase margin of 38 deg and a gain margin of 7.1 dB. The structural filter gain stabilizes the primary bending modes at 14 Hz with about 12-dB gain suppression.

Figure 5 shows the closed-loop frequency magnitude response of this new controller from the solar array disturbance input $d$ to the pitch attitude output $\theta$, along with that of the original controller (dotted line). As compared to the original controller, the new controller with two dipoles has achieved 40 dB more gain attenuation at both 0.12 and 0.66 Hz.

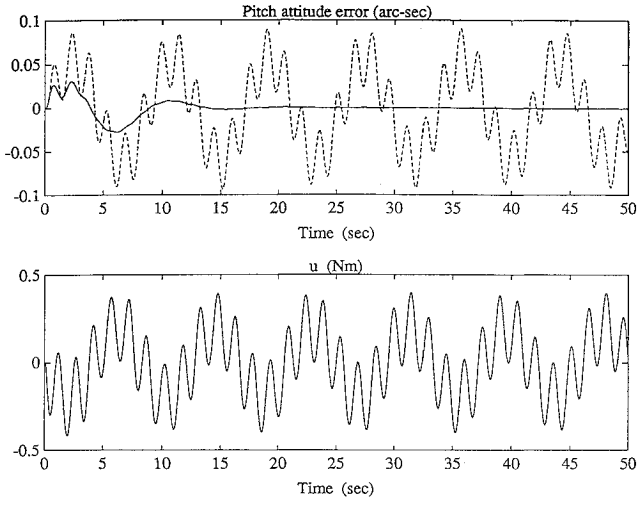


**Fig. 6 Time responses to $d(t) = 0.2\sin(2\pi p_1 t) + 0.2\sin(2\pi p_2 t)$ of a classical control redesign.**

The time responses to the solar array induced disturbances (in N-m)

$$d(t) = 0.2\sin[2\pi(0.12)t] + 0.2\sin[2\pi(0.66)t] \tag{9}$$

are shown in Fig. 6 along with the response of the original controller (dotted line). It can be seen that an effective rejection of the solar array disturbances at 0.12 and 0.66 Hz has been achieved, without exceeding the actuator limit of 2.5 N-m.

Such a simple classical approach based on a dipole concept[8] is a very effective means of achieving precision line-of-sight pointing control in the presence of significant structural vibrations or persistent external disturbances. It has been experimentally validated on the Mini-Mast truss structure at NASA Langley Research Center[9] and on the ACES testbed at NASA Marshall Space Flight Center[10] as part of the NASA Control Structure Interaction Phase I Guest Investigator Program. Such a simple concept is directly applicable to an image motion compensation problem,[11] and it has been proposed for the Space Station Freedom[12] to reduce the effects of the cyclic aerodynamic torques on attitude oscillation of the vehicle.

The classical approach, however, requires a significant amount of trial-and-error iterations to satisfy the 1.5-Hz bandwidth requirement and the stability requirements of the two dipoles and the rigid-body mode. In the next section, we will employ a modern state-space design technique based on $H_\infty$ control theory to overcome some drawbacks of a classical approach. It is, however, emphasized that even for such a modern systematic approach, trial-and-error iterations for selecting proper weightings are necessary in practice.

## IV. Robust $H_\infty$ Control Design

A robust $H_\infty$ control design methodology,[7] which is essentially based on state-space solutions of standard $H_\infty$ control problems,[13,14] is briefly summarized in Appendix B, with a special emphasis on modeling of both structured parametric uncertainty and unmodeled dynamics.[15-18] Many theoretical aspects of robust control are not elaborated in this section. Instead, we emphasize a proper formulation of the HST pointing control redesign problem for the robust $H_\infty$ control design in terms of structured and unstructured uncertainties.

The pole-zero pattern of the HST pitch-axis transfer function indicates that the pitch-axis dynamics can be approximated by a rigid-body mode and several dominant bending modes at 14 Hz. Since the control redesign requires gain stabilization of those bending modes with at least 6-dB gain suppression, the high-frequency bending modes are considered as unmodeled dynamics.

The pitch-axis dynamics of HST with only a rigid-body mode can then be described as

$$\frac{\mathrm{d}}{\mathrm{d}t}\begin{bmatrix}\theta\\ \dot\theta\end{bmatrix} = \begin{bmatrix}0 & 1\\ 0 & 0\end{bmatrix}\begin{bmatrix}\theta\\ \dot\theta\end{bmatrix} + \begin{bmatrix}0\\ 1+\delta\end{bmatrix}u + \begin{bmatrix}0\\ 1\end{bmatrix}d$$

$$y = \theta + v$$

where $\theta$ is the pitch attitude error, $d$ the external disturbance torque induced by solar arrays, $v$ the sensor noise, $u$ the pitch-axis control torque generated by reaction wheels, and $\delta$ represents a percentage variation of the overall loop gain perturbed mainly by vehicle inertia uncertainty (i.e., $\delta$ is a structured uncertain parameter).

As discussed in Appendix B, a fictitious input $\tilde d$ and a fictitious output $\tilde z$ are introduced as follows

$$\tilde d = \varepsilon u \qquad \tilde z = -u \qquad \varepsilon = \delta$$

where $\varepsilon$ is called the gain of a fictitious internal feedback loop.

Disturbance rejection filters are modeled as

$$\dot\alpha = y \tag{10a}$$

$$\ddot\beta_1 + p_1^2\beta_1 = y \tag{10b}$$

$$\ddot\beta_2 + p_2^2\beta_2 = y \tag{10c}$$

where $p_1 = 2\pi(0.12)$ rad/s and $p_2 = 2\pi(0.66)$ rad/s are the frequencies of solar array induced cyclic disturbances. Note that a constant-disturbance rejection filter is also included, since an integral compensation is needed to attenuate low-frequency disturbances.

The preceding disturbance model can be represented in state-space form as

$$\dot x_d = A_d x_d + B_d y \tag{11}$$

where

$$A_d = \begin{bmatrix}0 & 0 & 0 & 0 & 0\\ 0 & 0 & 1 & 0 & 0\\ 0 & -p_1^2 & 0 & 0 & 0\\ 0 & 0 & 0 & 0 & 1\\ 0 & 0 & 0 & -p_2^2 & 0\end{bmatrix}$$

$$B_d = \begin{bmatrix}1\\ 0\\ 1\\ 0\\ 1\end{bmatrix}, \qquad x_d = \begin{bmatrix}\alpha\\ \beta_1\\ \dot\beta_1\\ \beta_2\\ \dot\beta_2\end{bmatrix}$$

Finally, the state-space equation augmented by the disturbance model and the fictitious internal feedback loop can be described as:

$$\begin{aligned}\dot x(t) &= Ax(t) + B_1\hat d(t) + B_2u(t)\\ \hat z(t) &= C_1x(t) + D_{11}\hat d(t) + D_{12}u(t)\\ y(t) &= C_2x(t) + D_{21}\hat d(t) + D_{22}u(t)\end{aligned} \tag{12}$$

where

$$x = [\theta \quad \dot\theta \quad \alpha \quad \beta_1 \quad \dot\beta_1 \quad \beta_2 \quad \dot\beta_2]^T$$

$$\hat d = [\tilde d \quad d \quad v]^T, \qquad \hat z = [\tilde z \quad z]^T$$

$$A = \begin{bmatrix} 0 & 1 & 0 & 0 & 0 & 0 & 0 \\ 0 & 0 & 0 & 0 & 0 & 0 & 0 \\ 1 & 0 & 0 & 0 & 0 & 0 & 0 \\ 0 & 0 & 0 & 0 & 1 & 0 & 0 \\ 1 & 0 & 0 & -p_1^2 & 0 & 0 & 0 \\ 0 & 0 & 0 & 0 & 0 & 0 & 1 \\ 1 & 0 & 0 & 0 & 0 & -p_2^2 & 0 \end{bmatrix}$$

$$B_1 = \begin{bmatrix} 0 & 0 & 0 \\ 1 & 1 & 0 \\ 0 & 0 & 1 \\ 0 & 0 & 0 \\ 0 & 0 & 1 \\ 0 & 0 & 0 \\ 0 & 0 & 1 \end{bmatrix} W_{\hat{d}}, \qquad B_2 = \begin{bmatrix} 0 \\ 1 \\ 0 \\ 0 \\ 0 \\ 0 \\ 0 \end{bmatrix}$$

$$C_1 = \begin{bmatrix} 1 & 0 & w_\alpha & w_{\beta_1} & w_{\dot{\beta}_1} & w_{\beta_2} & w_{\dot{\beta}_2} \\ 0 & 0 & 0 & 0 & 0 & 0 & 0 \end{bmatrix}$$

$$C_2 = [1 \quad 0 \quad 0 \quad 0 \quad 0 \quad 0 \quad 0]$$

$$D_{12} = \begin{bmatrix} 0 \\ 1 \end{bmatrix}, \qquad D_{21} = [0 \quad 0 \quad 1]\, W_{\hat{d}}$$

and $D_{11} = 0$, $D_{22} = 0$; $W_{\hat{d}}$ is the diagonal weighting matrix for $\hat{d}$; $w_\alpha$, $w_{\beta_1}$, $w_{\dot{\beta}_1}$, $w_{\beta_2}$, and $w_{\dot{\beta}_2}$ are weighting factors for $\alpha$, $\beta_1$, $\dot{\beta}_1$, $\beta_2$, and $\dot{\beta}_2$, respectively.

*Remark:* In Eq. (12), $x$ denotes the augmented state vector, which consists of the plant state and the disturbance filter state, whereas $x$ denotes the plant state in Appendix B; however, the meaning of $x$ should be clear from the context.

The selection of a design bound $\gamma$ (see Appendix B) and various weighting factors requires a trial-and-error iteration for proper tradeoffs between performance and robustness. The weighting factors on the disturbance rejection filter states are related to the separation between corresponding pole and zero of a dipole. Such separation represents the strength of the dipole, which in turn affects the settling time of the closed-loop system.

After a certain amount of trial and error, we select

$$\gamma = 4.39$$

$$W_{\hat{d}} = \text{diag}\{0.05,\ 3.10,\ 0.002\}$$

$$w_\alpha = 0.3, \qquad w_{\beta_1} = 2.0, \qquad w_{\dot{\beta}_1} = 1.8$$

$$w_{\beta_2} = 0.5, \qquad w_{\dot{\beta}_2} = 20$$

Since all the structural modes are treated as unmodeled dynamics in the design process, we select the following weighting function

$$W(s) = \frac{0.532(s/30 + 1)^2}{\{[s/(2\pi \cdot 13.8)]^2 + 2(0.004)s/(2\pi \cdot 13.8) + 1\}} \tag{13}$$

to meet the frequency domain robustness requirement with respect to unstructured uncertainty (see Appendix B).

The Glover-Doyle algorithm[14] was then employed to find the following compensator:

$$K(s) = 5.945(1 + 0.063/s + 1.683s)R(s)S(s) \tag{14}$$

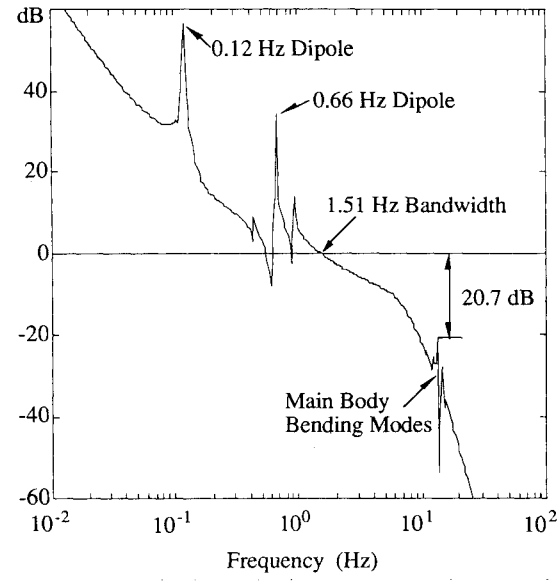


**Fig. 7 Bode magnitude plot of the loop transfer function of a robust $H_\infty$ control redesign.**

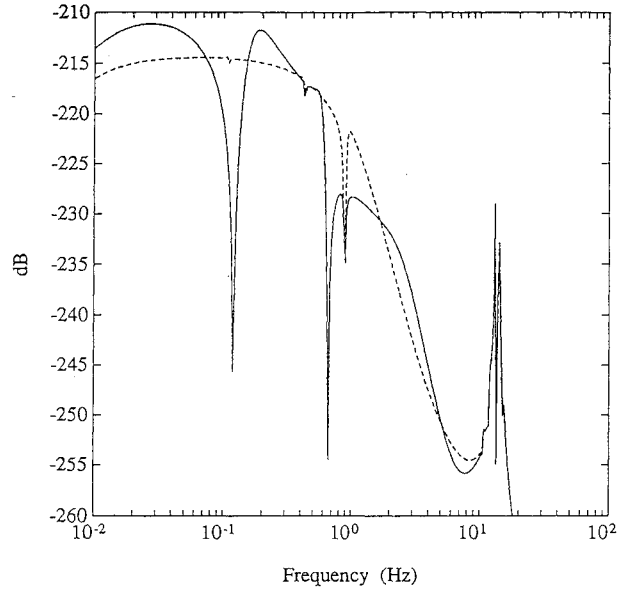


**Fig. 8 Closed-loop frequency magnitude response of a robust $H_\infty$ control redesign.**

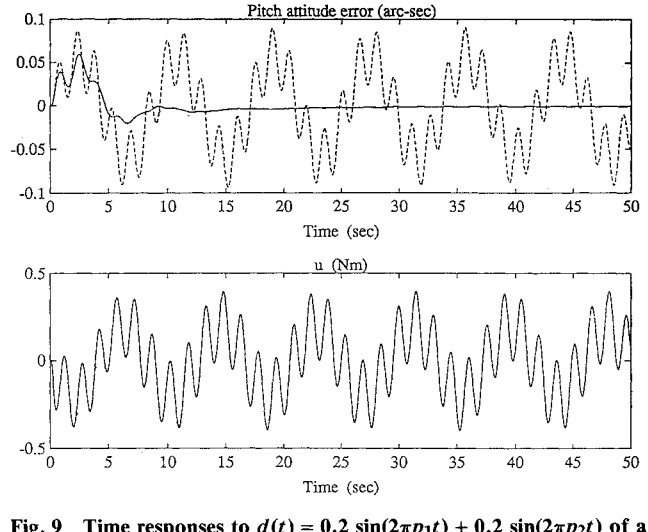


**Fig. 9 Time responses to $d(t) = 0.2 \sin(2\pi p_1 t) + 0.2 \sin(2\pi p_2 t)$ of a robust $H_\infty$ control redesign.**

where

$$R(s) = \frac{[(s/0.946)^2 + 2(0.283)s/0.946 + 1]}{[(s/0.754)^2 + 1]} \times \frac{[(s/3.746)^2 + 2(0.021)s/3.746 + 1]}{[(s/4.147)^2 + 1]} \quad (15)$$

$$S(s) = \frac{[(s/86.71)^2 + 2(0.004)s/86.71 + 1]}{[(s/42.76)^2 + 2(0.454)s/42.76 + 1]} \times \frac{1}{[(s/58.40)^2 + 2(0.862)s/58.40 + 1]} \quad (16)$$

where $R(s)$ and $S(s)$ are referred to as the disturbance rejection filter and the structural filter, respectively. For an effective rejection of the sinusoidal disturbances, the filter $R(s)$ has poles at $\pm 2\pi(0.12)j$ and $\pm 2\pi(0.66)j$ with the associated zeros at $-0.267 \pm 0.907j$ and $-0.079 \pm 3.745j$, respectively. (Such a pole-zero pair is called a disturbance rejection dipole.[8])

The Bode magnitude plot of the loop transfer function with this new controller is shown in Fig. 7. As can be seen in this figure, this new controller has met the bandwidth requirement of 1.5-Hz gain crossover frequency. It has a 5.1-dB gain margin and a 37-deg phase margin. The notch zeros at 13.8 Hz provide effective gain stabilization of the primary bending modes at 14 Hz with about 21-dB gain suppression. The closed-loop frequency magnitude response of this new controller from the solar array disturbance input $d$ to the pitch attitude output $\theta$ is compared with that of the original controller (dotted line) in Fig. 8. It can be seen that this new controller has achieved additional 40-dB disturbance attenuation at both 0.12 and 0.66 Hz with respect to the original controller. Such an effective rejection of the disturbances can also be seen in time responses shown in Fig. 9.

## V. Conclusions

Both classical and robust $H_\infty$ control synthesis techniques were applied to a control redesign problem of the Hubble Space Telescope. It was demonstrated that the proposed controllers with two disturbance rejection dipoles effectively accommodate the solar array induced disturbances at 0.12 and 0.66 Hz, resulting in a significant pointing performance improvement over the original controller on board the Hubble Space Telescope. Some practical usefulness of a modern, but somewhat esoteric, robust $H_\infty$ control design methodology has been also demonstrated, although trial-and-error iterations for selecting proper weightings were necessary.

## Appendix A: Classical Control Synthesis

### Successive-Mode Stabilization

The design of a single-input and single-output (SISO) feedback control system for a flexible spacecraft is carried out starting with the stabilization of a rigid-body mode and subsequent analysis and stabilization of any unstably interacting flexible modes. Feedback control with a noncollocated actuator and sensor pair or with significant time delay generally results in the presence of unstably interacting flexible modes. After the unstably interacting modes have been identified, proper filtering to phase or gain stabilize those modes is then introduced. Also, active disturbance rejection filtering is synthesized to compensate for any persistent disturbances acting on the spacecraft. Aided by the root locus method and/or Bode plots, and a certain amount of trial and error, a robust compensator design is performed. The classical SISO design based on successive-mode stabilization can be divided into four steps: 1) stabilization of a rigid-body mode according to given time- or frequency-domain specifications (settling time, maximum overshoot, bandwidth, phase, and gain margins); 2) gain/phase stabilization of any unstably interacting or destabilized flexible modes; 3) synthesis of active disturbance rejection filter and/or command preshaping filter; and 4) final tuning of the overall compensator. The last step becomes necessary because the phase and gain characteristics of active disturbance rejection filtering as well as the stabilized modes in question exert their influence on all of the neighboring frequencies, which may include other modes. This presents a challenge as the number of modes to be stabilized becomes larger.

Phase and/or gain stabilization of an unstably interacting flexible mode can be achieved with the introduction of a roll-off filter and/or a generalized second-order filter of the following form in the feedback loop:

$$\frac{(s/z)^2 + 2\zeta_z s/z + 1}{(s/p)^2 + 2\zeta_p s/p + 1}$$

where $s$ is the Laplace transform variable. Nonminimum-phase second-order shaping filters with negative $\zeta_z$ are of special interest for a certain class of noncollocated control problems, as discovered in Ref. 6.

### Active Disturbance Rejection

After successful stabilization of the rigid-body mode (as well as any other unstably interacting flexible modes), active disturbance rejection is then simply achieved by introducing into the feedback loop a disturbance model of the form

$$d(t) = \sum_i A_i \sin(p_i t + \phi_i)$$

with unknown magnitudes $A_i$ and phases $\phi_i$ but known frequencies $p_i$. In general, the disturbance $d(t)$ can be described by a Laplace transformation $d(s) = N_d(s)/D_d(s)$, where $N_d(s)$ is arbitrary as long as $d(s)$ remains proper. The roots of $D_d(s)$ correspond to the frequencies at which the persistent excitation takes place. The inclusion of the disturbance model $1/D_d$ inside the control loop is often referred to as the internal modeling of the disturbance.

As shown in Fig. A1, the presence of $1/D_d$ in the control loop results in the effective cancellation of the poles of $d(s)$, provided that no root of $D_d(s)$ is a zero of the plant transfer function. This is shown in the following closed-loop transfer function:

$$y(s) = \frac{1/D(s)}{1 + N_c(s)N(s)/D_c(s)D_d(s)D(s)} d(s) = \frac{D_c(s)D_d(s)}{D_d(s)D_c(s)D(s) + N_c(s)N(s)} \frac{N_d(s)}{D_d(s)}$$

where we can see the cancellation of $D_d(s)$.

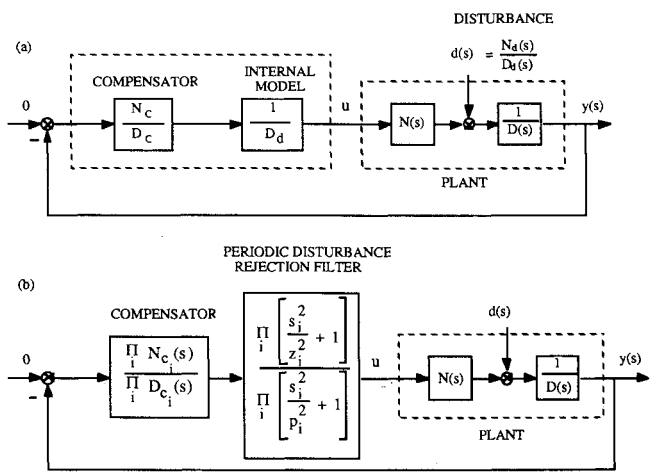


**Fig. A1 Block diagram representation of a disturbance rejection controller.**

The compensator can be viewed as a series of individual first-order or second-order filters as follows:

$$\frac{N_c(s)}{D_c(s)} = \prod_i \frac{N_{c_i}(s)}{D_{c_i}(s)}$$

Each filter is designed to perform a specific task, like the stabilization of a particular mode. In the same manner, a disturbance rejection filter can be designed that has a proper transfer function and uses the internal disturbance model $1/D_d$. Thus a proper numerator is chosen in the compensator to go with the disturbance model. The numerator is chosen to be of the same order as $D_d$ so that there is a zero for each pole of the disturbance model $1/D_d$.

Each pole-zero combination of the disturbance rejection filter

$$\prod_i \frac{(s/z_i)^2 + 2\zeta_{z_i} s/z_i + 1}{(s/p_i)^2 + 1}$$

can be called a dipole, where $\zeta_{z_i}$ is included for generality. The filter thus consists of as many dipoles as there are frequency components in the persistent disturbance. The separation between the zero and the pole is generally referred to as the strength of the dipole. The strength of the dipole affects the settling time of the closed-loop system; in general, the larger the separation between the pole and zero of the filter the shorter the settling time. This is caused by the position of the closed-loop eigenvalue corresponding to the filter dipole. As the strength of the dipole is increased, this eigenvalue is pushed farther to the left, speeding up the response time of the disturbance rejection. Therefore, as the strength of the dipole is changed to meet a chosen settling time the rigid and flexible mode compensation logic must be readjusted. A compromise has to be reached often between the the settling time and the stability of the compensated system.

## Appendix B: Robust $H_\infty$ Control Synthesis

### Modeling of Structured Uncertainty

Consider a flexible spacecraft described by

$$M\ddot{q} + D\dot{q} + Kq = G_d d + G_u u \tag{B1}$$

where $q$ is a generalized displacement vector, $M$ a mass matrix, $D$ a damping matrix, $K$ a stiffness matrix, $G_d$ the disturbance distribution matrix, $G_u$ the control input distribution matrix, $d$ the external disturbance vector, and $u$ the control input vector.

Suppose that matrices $M$, $D$, and $K$ are subject to $\ell$ independent parameter variations, $\delta_i$ $(i = 1, \ldots, \ell)$. The perturbed matrices in Eq. (B1) can then be linearly decomposed as

$$\begin{aligned} M &= M_0 + \Delta M \\ D &= D_0 + \Delta D \\ K &= K_0 + \Delta K \end{aligned} \tag{B2}$$

The first matrices on the right-hand side of Eq. (B2) are the nominal matrices and the second ones are the perturbation matrices that are decomposed as

$$\begin{aligned} \Delta M &= \mathfrak{M}_M \mathcal{E}_M \mathfrak{N}_M \\ \Delta D &= \mathfrak{M}_D \mathcal{E}_D \mathfrak{N}_D \\ \Delta K &= \mathfrak{M}_K \mathcal{E}_K \mathfrak{N}_K \end{aligned} \tag{B3}$$

where $\mathcal{E}_M$, $\mathcal{E}_D$, and $\mathcal{E}_K$ are diagonal matrices with independent parameter variations $\delta_i$ as diagonal elements.

Defining

$$\mathcal{E} \triangleq \operatorname{diag}\{\mathcal{E}_M, \mathcal{E}_D, \mathcal{E}_K\} \tag{B4a}$$

$$\tilde{z} \triangleq \begin{bmatrix} \tilde{z}_M \\ \tilde{z}_D \\ \tilde{z}_K \end{bmatrix} = \begin{bmatrix} \mathfrak{N}_M \ddot{q} \\ \mathfrak{N}_D \dot{q} \\ \mathfrak{N}_K q \end{bmatrix} \tag{B4b}$$

$$\tilde{d} \triangleq -\mathcal{E}\tilde{z} \tag{B4c}$$

and substituting Eq. (B2) into Eq. (B1), we get

$$M_0\ddot{q} + D_0\dot{q} + K_0 q = G_{\tilde{d}}\tilde{d} + G_d d + G_u u \tag{B5}$$

where

$$G_{\tilde{d}} = [\mathfrak{M}_M, \mathfrak{M}_D, \mathfrak{M}_K] \tag{B6}$$

and where $\tilde{d}$ is the fictitious input, $\tilde{z}$ the fictitious output, $\mathcal{E}$ the gain matrix of a fictitious internal feedback loop, and $G_{\tilde{d}}$ the fictitious disturbance distribution matrix.

After defining the state vector and controlled output vector as

$$x = \begin{bmatrix} q \\ \dot{q} \end{bmatrix} \tag{B7a}$$

$$z = \begin{bmatrix} C_{11} & C_{12} \\ 0 & 0 \end{bmatrix} \begin{bmatrix} q \\ \dot{q} \end{bmatrix} + \begin{bmatrix} 0 \\ I \end{bmatrix} u \tag{B7b}$$

where $I$ is a unit matrix with proper dimension, and introducing new variables

$$\hat{d} = \begin{bmatrix} \tilde{d} \\ d \\ v \end{bmatrix} \qquad \hat{z} = \begin{bmatrix} \tilde{z}_M \\ \tilde{z}_D \\ \tilde{z}_K \\ z \end{bmatrix}$$

where $v$ is the sensor noise vector, we obtain the following modified state-space representation of the system as

$$\begin{aligned} \dot{x}(t) &= Ax(t) + B_1\hat{d}(t) + B_2 u(t) \\ \hat{z}(t) &= C_1 x(t) + D_{11}\hat{d}(t) + D_{12}u(t) \\ y(t) &= C_2 x(t) + D_{21}\hat{d}(t) + D_{22}u(t) \end{aligned} \tag{B8}$$

where

$$A = \begin{bmatrix} 0 & I \\ -M_0^{-1}K_0 & -M_0^{-1}D_0 \end{bmatrix}$$

$$B_1 = \begin{bmatrix} 0 & 0 & 0 \\ M_0^{-1}G_{\tilde{d}} & M_0^{-1}G_d & 0 \end{bmatrix}, \qquad B_2 = \begin{bmatrix} 0 \\ M_0^{-1}G_u \end{bmatrix}$$

$$C_1 = \begin{bmatrix} -\mathfrak{N}_M M_0^{-1}K_0 & -\mathfrak{N}_M M_0^{-1}D_0 \\ 0 & \mathfrak{N}_D \\ \mathfrak{N}_K & 0 \\ C_{11} & C_{12} \\ 0 & 0 \end{bmatrix}$$

$$D_{11} = \begin{bmatrix} \mathfrak{N}_M M_0^{-1}G_{\tilde{d}} & \mathfrak{N}_M M_0^{-1}G_d & 0 \\ 0 & 0 & 0 \end{bmatrix}$$

$$D_{12} = \begin{bmatrix} \mathfrak{N}_M M_0^{-1}G_u \\ 0 \\ I \end{bmatrix}$$

and $D_{21} = D_{22} = 0$. Note that $D_{11} = 0$ if there is no uncertainty in the mass matrix $M$.

**Modeling of Unstructured Uncertainty**

Consider an uncertain system described as

$$G(s, \delta) + \Delta G(s) \tag{B9}$$

or

$$[I + \Delta G(s)]G(s,\delta) \tag{B10}$$

where $\delta \in \mathfrak{D}$ denotes a structured uncertain parameter vector, and $\Delta G(s)$ represents unstructured uncertainty, which can be modeled as additive uncertainty in Eq. (B9) or multiplicative uncertainty in Eq. (B10).

A stability criterion in the presence of both structured parameter variation and unmodeled dynamics is given as follows.[16-18]

*Theorem (Robust Stability):* If $K(s)$ stabilizes $G(s,\delta)$ for all $\delta \in \mathfrak{D}$, then $K(s)$ stabilizes $G(s,\delta) + \Delta G(s)$ if

$$\|\Delta G(s)\|_\infty < \frac{1}{\|K(s)[I + G(s,\delta)K(s)]^{-1}\|_\infty} \tag{B11}$$

for all $\delta \in \mathfrak{D}$.

Similarly, if $K(s)$ stabilizes $G(s,\delta)$ for all $\delta \in \mathfrak{D}$, then $K(s)$ stabilizes $[I + \Delta G(s)]G(s,\delta)$ if

$$\|\Delta G(s)\|_\infty < \frac{1}{\|G(s,\delta)K(s)[I + G(s,\delta)K(s)]^{-1}\|_\infty} \tag{B12}$$

for all $\delta \in \mathfrak{D}$.

The design problem is then to find a robustly stabilizing controller that minimizes

$$\|W(s)K(s)[I + G(s,\delta)K(s)]^{-1}\|_\infty \tag{B13}$$

for additive uncertainty, or

$$\|W(s)G(s,\delta)K(s)[I + G(s,\delta)K(s)]^{-1}\|_\infty \tag{B14}$$

for multiplicative uncertainty. The frequency-dependent weighting function $W(s)$ is properly selected in accordance with the available information on unmodeled dynamics. The closed-loop system will then be robustly stable in the presence of both structured uncertainty and unmodeled dynamics.

Considering both an internal feedback loop model for structured parameter variations and a weighting function for unmodeled dynamics, we have the following state-space representation of an uncertain system:

$$\begin{bmatrix} \dot{x} \\ \dot{x}_w \end{bmatrix} = \begin{bmatrix} A & 0 \\ 0 & A_w \end{bmatrix} \begin{bmatrix} x \\ x_w \end{bmatrix} + \begin{bmatrix} B_1 \\ 0 \end{bmatrix} \hat{d} + \begin{bmatrix} B_2 \\ B_w \end{bmatrix} u \tag{B15a}$$

$$\begin{bmatrix} \hat{z} \\ z_w \end{bmatrix} = \begin{bmatrix} C_1 & 0 \\ 0 & C_w \end{bmatrix} \begin{bmatrix} x \\ x_w \end{bmatrix} + \begin{bmatrix} D_{11} \\ 0 \end{bmatrix} \hat{d} + \begin{bmatrix} D_2 \\ D_w \end{bmatrix} u \tag{B15b}$$

$$y = [C_2 \quad 0] \begin{bmatrix} x \\ x_w \end{bmatrix} + D_{21}\hat{d} + D_{22}u \tag{B15c}$$

where

$$W(s) = :(A_w, B_w, C_w, D_w) \tag{B16}$$

and $x_w$ is the state vector associated with the weighting function.

**Robust Asymptotic Disturbance Rejection**

A state-space model of an uncertain system of the preceding section is now further augmented by the internal model of the disturbances.

Consider a persistent disturbance with one or more frequency components represented as

$$d(t) = \sum_i A_i \sin(p_i t + \phi_i)$$

with unknown magnitudes $A_i$ and phases $\phi_i$ but known frequencies $p_i$. Active disturbance rejection for the measured output is achieved by introducing a model of the disturbance inside the control loop. A disturbance rejection filter for $d_i(t)$ at a particular frequency $p_i$ is then modeled as

$$\dot{x}_{d_i} = A_{d_i} x_{d_i} + B_{d_i} y \tag{B17}$$

where

$$A_{d_i} = \begin{bmatrix} 0 & 1 \\ -p_i^2 & 0 \end{bmatrix}; \qquad B_{d_i} = \begin{bmatrix} 0 \\ 1 \end{bmatrix}$$

The internal model then includes as many frequencies as the given disturbance and is driven by the measured output $y$ of the plant. This procedure is equivalent to the one used in the classical approach with the disturbance model now consisting of a state-space model. The disturbance rejection filter is then described by

$$\dot{x}_d = A_d x_d + B_d y \tag{B18}$$

where $x_d$ is the state vector introduced by the internal disturbance model, $A_d$ is block-diagonal and contains $A_{d_i}$ for each disturbance $d_i(t)$, and $B_d$ also contains $B_{d_i}$ for each disturbance.

The disturbance filter model described by Eq. (B18) is then augmented to Eqs. (B15) as follows:

$$\begin{bmatrix} \dot{x} \\ \dot{x}_d \\ \dot{x}_w \end{bmatrix} = \begin{bmatrix} A & 0 & 0 \\ B_d C_2 & A_d & 0 \\ 0 & 0 & A_w \end{bmatrix} \begin{bmatrix} x \\ x_d \\ x_w \end{bmatrix} + \begin{bmatrix} B_1 \\ B_d D_{21} \\ 0 \end{bmatrix} \hat{d} + \begin{bmatrix} B_2 \\ 0 \\ B_w \end{bmatrix} u \tag{B19a}$$

$$\begin{bmatrix} \hat{z} \\ z_w \end{bmatrix} = \begin{bmatrix} C_1 & W_d & 0 \\ 0 & 0 & C_w \end{bmatrix} \begin{bmatrix} x \\ x_d \\ x_w \end{bmatrix} + \begin{bmatrix} D_{11} \\ 0 \end{bmatrix} \hat{d} + \begin{bmatrix} D_2 \\ D_w \end{bmatrix} u \tag{B19b}$$

$$y = [C_2 \quad 0 \quad 0] \begin{bmatrix} x \\ x_d \\ x_w \end{bmatrix} + D_{21}\hat{d} + D_{22}u \tag{B19c}$$

where $W_d$ is a relative weighting factor for $x_d$.

**Robust $H_\infty$ Control Design**

Given a state-space model of a generalized plant, given by Eqs. (B19), the Glover-Doyle algorithm[14] is employed to obtain a robust $H_\infty$ controller such that

$$\|T_{\bar{z}\hat{d}}\|_\infty < \gamma \tag{B20}$$

where $\bar{z} = [\hat{z}^T, z_w^T]^T$. The stability and performance robustness with respect to both structured uncertainty and unmodeled dynamics is guaranteed for such a controller.[7,15-18]

The robust $H_\infty$ control methodology employed in this paper incorporates the internal model principle for asymptotic disturbance rejection in the presence of persistent external disturbances. Since the states of the disturbance rejection filter and the weighting function are not detectable from the measured

output, a very small artificial damping (about 0.0001) is needed for pure imaginary poles for the convenience of avoiding numerical problems in solving two Riccati equations.

## Acknowledgments

This research was supported in part by the NASA Langley Research Center under the Control Structure Interaction (CSI) Phase I Guest Investigator Program and by the NASA Goddard Space Flight Center. The authors would like to thank Harry Frisch of NASA Goddard and Jerry Newsom and Rudeen Smith-Taylor of NASA Langley for their support in this research. The authors are also very grateful to John Sharkey of the NASA Marshall Space Flight Center and Michael Femiano of NASA Goddard for their technical assistance for understanding the HST control redesign problem.

## References

[1]Dougherty, H., Tompetrini, K., Levinthal, J., and Nurre, G., "Space Telescope Pointing Control System," *Journal of Guidance, Control, and Dynamics,* Vol. 5, No. 4, 1982, pp. 403–409.

[2]Beals, G. A., Crum, R. C., Dougherty, H. J., Hegel, D. K., Kelley, J. L., and Rodden, J. J., "Hubble Space Telescope Precision Pointing Control System," *Journal of Guidance, Control, and Dynamics,* Vol. 11, No. 2, 1988, pp. 119–123.

[3]"Hubble Space Telescope SAGA Readiness Review Report," NASA Goddard Space Flight Center, Greenbelt, MD, Oct. 2, 1990.

[4]Sharkey, J. P.,"A SAGA/Ga Controller with Increased Attenuation at 0.6 Hz," Internal Memo, NASA Marshall Space Flight Center, June 4, 1991.

[5]Bryson, A. E., Jr., *Control of Aircraft and Spacecraft,* Stanford Univ., Stanford, CA, Dec. 31, 1990, Chap. 9.

[6]Wie, B., and Byun, K., "New Generalized Structural Filtering Concept for Active Vibration Control Synthesis," *Journal of Guidance, Control, and Dynamics,* Vol. 12, No. 2, 1989, pp. 147–154.

[7]Wie, B., Liu, Q., and Byun, K.-W., "Robust $H_\infty$ Control Synthesis Method and Its Application to Benchmark Problems," *Journal of Guidance, Control, and Dynamics,* Vol. 15, No. 5, 1992, pp. 1140–1148.

[8]Wie, B., and Gonzalez, M., "Control Synthesis for Flexible Space Structures Excited by Persistent Disturbances," *Journal of Guidance, Control, and Dynamics,* Vol. 15, No. 1, 1992, pp. 73–80.

[9]Wie, B., Horta, L., and Sulla, J., "Classical Control System Design and Experiment for the Mini-Mast Truss Structure," *Journal of Guidance, Control, and Dynamics,* Vol. 14, No. 4, 1991, pp. 778–784.

[10]Wie, B., "Experimental Demonstration of a Classical Approach to Flexible Structure Control: The ACES Testbed," *Journal of Guidance, Control, and Dynamics,* Vol. 15, No. 6, 1992, pp. 1327–1333.

[11]Bauer, F. H., and Deily, J. J., "Image Motion Compensation for the Ultraviolet Imaging Telescope," *Proceedings of the AIAA Guidance, Navigation, and Control Conference,* AIAA, Washington, DC, 1990, pp. 1011–1021.

[12]Wie, B., Byun, K. W., Warren, V. W., Geller, D., Long, D., and Sunkel, J., "New Approach to Attitude/Momentum Control of the Space Station," *Journal of Guidance, Control, and Dynamics,* Vol. 12, No. 5, 1989, pp. 714–722.

[13]Glover, K., and Doyle, J., "State-Space Formulae for All Stabilizing Controllers that Satisfy an $H_\infty$-norm Bound and Relations to Risk Sensitivity," *System and Control Letters,* Vol. 11, 1988, pp. 167–172.

[14]Doyle, J., Glover, K., Khargonekar, P., and Francis, B., "State-Space Solutions to Standard $H_2$ and $H_\infty$ Control Problems," *IEEE Transactions on Automatic Control,* Vol. AC-34, No. 8, 1989, pp. 831–847.

[15]Doyle, J. C., and Stein, "Multivariable System Design: Concepts for a Classical/Modern Synthesis," *IEEE Transactions on Automatic Control,* Vol. AC-26, No. 1, Feb. 1981, pp. 4–16.

[16]Wei, K., and Yedavalli, R. K.,"Robust Stability for Linear Systems with Both Parameter Variation and Unstructured Uncertainty," *IEEE Transactions on Automatic Control,* Vol. AC-34, No. 2, 1989, pp. 149–155.

[17]Yeh, H.-H., Banda, S. S., Heise, and Bartlett, A. C., "Robust Control Design with Real-Parameter Uncertainty and Unmodeled Dynamics," *Journal of Guidance, Control, and Dynamics,* Vol. 13, No. 6, 1990, pp. 1117–1125.

[18]Fan, M. K. H., Tits, A. L., and Doyle, J. C., "Robustness in the Presence of Mixed Parameteric Uncertainty and Unmodeled Dynamics," *IEEE Transactions on Automatic Control,* Vol. AC-36, No. 1, 1991, pp. 25–38.